

Characterization of the Hamamatsu 8-inch R14688-100 PMT

Tanner Kaptanoglu^{1,2} Ashley Rincon¹ Mackenzie Duce⁴ Sawyer Kaplan¹ Joseph Koplowitz¹ Skipper Lynch³ Hong Joo Ryoo¹ Gabriel Orebi Gann^{1,2}

¹*University of California, Berkeley, 366 Physics North, Berkeley, CA 94720-7300*

²*Lawrence Berkeley National Laboratory, 1 Cyclotron Rd, Berkeley CA 94720-8153*

³*Massachusetts Institute of Technology, 77 Massachusetts Avenue, Cambridge, MA 02139-4307*

⁴*Georgia Institute of Technology, 801 Ferst Drive, Atlanta, GA 30332-0315*

ABSTRACT: Large-scale optical neutrino and dark-matter detectors rely on large-area photomultiplier tubes (PMTs) for cost-effective light detection. The new R14688-100 8-inch PMT developed by Hamamatsu provides state-of-the-art timing resolution of around 1 ns (FWHM), which can help improve vertex reconstruction and enable Cherenkov and scintillation light separation in scintillation-based detectors. This PMT also provides excellent charge resolution, allowing for precision photoelectron counting and improved energy reconstruction. The Eos experiment is the first large-scale optical detector to utilize these PMTs. In this manuscript we present a characterization of the R14688-100 single photoelectron response, such as the transit-time spreads, the dark-rates, and the afterpulsing. The single photoelectron response measurements are performed for the 206 PMTs that will be used in Eos.

KEYWORDS: Photomultiplier tube, Eos, neutrino detectors

Contents

1	Introduction	1
2	R14688-100 PMT	2
3	SPE Characterization	2
3.1	Experimental Setup	2
3.2	Analysis	4
3.3	Results	4
3.3.1	Charge	4
3.3.2	Timing	5
3.3.3	High Voltage Scan	6
3.3.4	Dark-Rate	7
3.3.5	SPE summary	7
4	Afterpulsing	7
4.1	Experimental Setup	7
4.2	Analysis	8
4.3	Results	8
5	Radiopurity Assay	10
6	Discussion	10
7	Conclusion	11
8	Acknowledgements	11
A	Magnetic Shielding Tests	12
A.1	Experimental Setup	12
A.2	Analysis	13
A.3	Results	13
B	List of Results for All PMTs	15

1 Introduction

Large-area photomultiplier tubes (PMTs) have been used in dozens of optical neutrino and direct dark-matter experiments [1–5] as an effective and cost efficient way of effectively covering large surface areas with photo-sensitive detectors. An understanding of the availability and performance

of different large-area PMTs is crucial for future experiments, such as THEIA [6], in the selection of sensors [7], as well as for accurately simulating the PMT response in existing detectors. The R14688-100 is one such large-area PMT, that will be used for the first time in a large-scale experiment in the Eos detector [8].

Eos is a 20-ton detector, designed to perform a demonstration of key technology for future advanced neutrino detectors [8] that plan to distinguish Cherenkov and scintillation light. This technology includes spectral sorting of photons [9], novel types of liquid scintillators [10, 11], and fast timing photodetectors [12]. The R14688-100 PMT from Hamamatsu was primarily selected for use in the Eos experiment due to its excellent timing resolution of around 1 ns FWHM [13]. This can be compared to other PMTs of similar size that have timing resolutions around 2 to 3 ns [13–16]. This fast timing is an important aspect in Cherenkov and scintillation separation, and it also helps to improve vertex reconstruction in optical photon-based large-scale neutrino detectors.

A total of 206 of these PMTs were purchased to be used in Eos. The experiment requires precise characterization of each PMT to verify they each meet the detector standard in a variety of metrics. In this manuscript, we characterize the properties of these 206 PMTs. In detectors the size of Eos and larger, the PMTs primarily detect single photons within a given event window, and thus the single photoelectron (SPE) response is critical to determine. We also investigate the dark-rate of several PMTs, the afterpulsing rate of a single PMT, and present measurements of the PMT radio purity. These measured characteristics are additionally used in precision modeling of Eos in the RAT-PAC simulation software [17].

2 R14688-100 PMT

The R14688-100 Hamamatsu PMT is 202 mm in diameter with a high quantum efficiency, super-bialkali photocathode and an expected transit time spread (TTS) of around 1 ns full width at half maximum (FWHM) [13]. The neck and base of the PMTs are by default water-proof potted and cabled by Hamamatsu (20 meter water proof cabling). The dynode is 10 stages and is box and linear-focused. A picture of the PMT is shown in Figure 1.

3 SPE Characterization

3.1 Experimental Setup

The experimental setup to measure the SPE response of the PMTs consists of a central UV-transparent, cylindrical acrylic vessel (AV) which is 3 cm tall and 3 cm in diameter. A ^{90}Sr β source is placed above the acrylic vessel. The β particles enter the acrylic and produce Cherenkov light. A Hamamatsu H11934-200 1-inch square PMT is optically coupled to the acrylic vessel using Eljin Technology EJ-550 optical grease.

Two R14688-100 ‘measurement’ PMTs are placed 20 cm on either side of the AV. The distance is selected to limit the coincidence rate between the trigger PMT and the measurement PMTs to below 5%, which ensures we are primarily detecting SPEs. The PMTs are wrapped in a one layer of magnetic shielding that spans from the base of the PMT (where the cable exits) to the equator. The magnetic shielding protects against the Earth’s magnetic field, which can deflect the photoelectrons as they travel inside of the PMT, affecting the overall collection efficiency. The strength of the



Figure 1. The R14688-100 PMT with the black water-proof potting and the 20 meter SHV cable.

magnetic field in the darkbox is approximately $50 \mu\text{T}$, but is reduced by about a factor of 5 inside of the magnetic shielding. Further discussion of the magnetic shielding is provided in [A](#).

A picture of the SPE testing setup is shown in [Figure 2](#). The space limitation of the darkbox limits the testing to two PMTs at a time. The high voltage (HV) for each PMT is selected such that the gain of the PMT is 1×10^7 . All measurements are performed at room temperature.

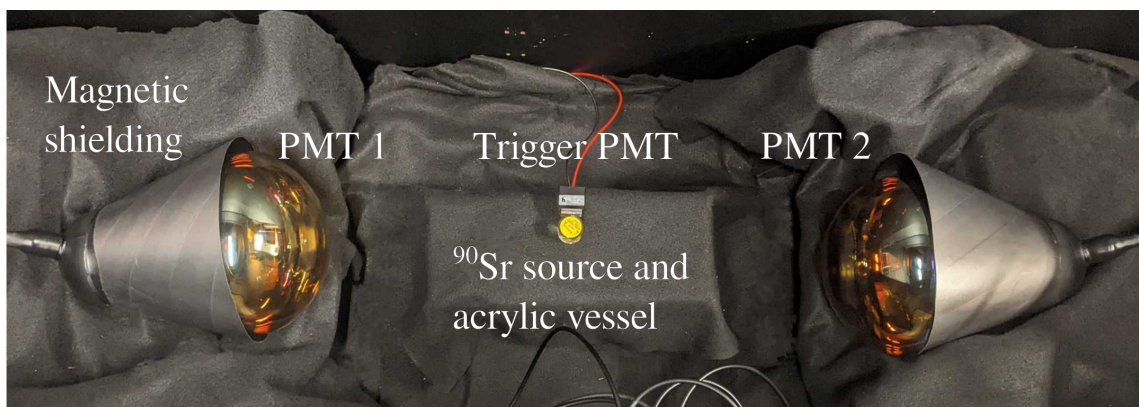


Figure 2. The experimental setup to measure the SPE response of the R14688-100 PMTs.

The signal from the trigger PMT is used to start the data acquisition (DAQ). Custom software reads out a V1742 CAEN waveform digitizer, which digitizes the signals from each of the PMTs. The sampling rate of the digitizer is 5 GHz over 1024 samples and it has 12-bit ADC over a 1 V dynamic range. The waveforms for each channel are saved to an hdf5 files. A total of 500,000 total triggers are collected, which ensures that the statistical uncertainties on the measured timing

characteristics are less than 5%.

3.2 Analysis

The data analysis code processes the hdf5 files output by the DAQ. First, a per-channel baseline is calculated by averaging over a 40 ns pre-trigger window. Then, for each channel, the minimum voltage is identified (the PMT pulses are downward going) and is referred to as the ‘peak’. The total charge deposited, Q , is calculated by integrating the PMT pulse in a dynamic window that ranges [-6, 12] ns around the peak of the pulse. This calculation is also performed for the trigger PMT.

Prior to calculating the timing, events above a threshold of about 0.2 PE are selected by enforcing $Q > 0.3$. As discussed in Section 3, this removes less than 5% of the SPE pulses.

The time of the measurement PMT pulse is calculated by applying a software-based constant fraction discriminator, linearly interpolating between the samples. The fractional threshold is set to 20%, but the precise value selected does not impact the results. For the trigger PMT, which detects many PEs per event, the time associated with a constant 2 mV threshold crossing (again, applying inter-sample interpolation) is used. This method identifies the time of the first PE detected by the trigger PMT and is more robust to the shape fluctuations in the multi-PE (MPE) pulses.

The time-difference between the measurement PMT time and the trigger PMT time, Δt , is used to extract the timing characteristics of the measurement PMT. The trigger PMT effectively acts to produce a time-zero that has a very small jitter of about 270 ps (FWHM) [18], which add negligibly to any jitter in the timing of the R14688-100 PMTs (which we expect to be around 1 ns FWHM).

3.3 Results

3.3.1 Charge

The charge distribution for the PMT with serial number VA1206 is shown in Figure 3. The ‘pedestal’ peak centered around 0 pC (which extends outside of the y-axis on the figure) corresponds to empty waveforms with no detected photon. This comprises the vast majority of the coincidences, as the coincidence rate is selected to be below 5%. The peak around 1.6 pC corresponds to the detection of single photons with a gain of 1×10^7 . The value of the peak is determined by identifying the maximum bin above 0.2 pC and fitting a Gaussian over the range that is 0.4 pC on either side of the peak.

As identifiable in Figure 3 the one PE peak is well separated from the zero PE peak. This is often quantified using a peak-to-valley (P/V) ratio. The P/V is calculated by identifying the total counts in the peak bin and dividing by the total counts in bin at 0.5 pC. The selection of this value is arbitrary, but it allows for a stable definition that is not impacted by small changes in the width of the baseline peak around 0 pC. The P/V for VA1206 is 4.58, and the PMTs typically have values above 4. This can be compared directly to other types of large-area PMTs, which have values around 2 to 3 [14, 19].

Because the P/V is so large for these PMTs, relatively few PMT pulses fall below the 0.3 pC threshold applied for the timing measurement, described below. If the charge distribution extrapolates linearly down to 0 pC under the pedestal, less than 5% of the SPE pulses are lost from the roughly 0.2 PE threshold. This highlights the advantage of the large P/V ratio for these PMTs, indicating that any threshold applied below the peak will have a relatively small efficiency sacrifice.

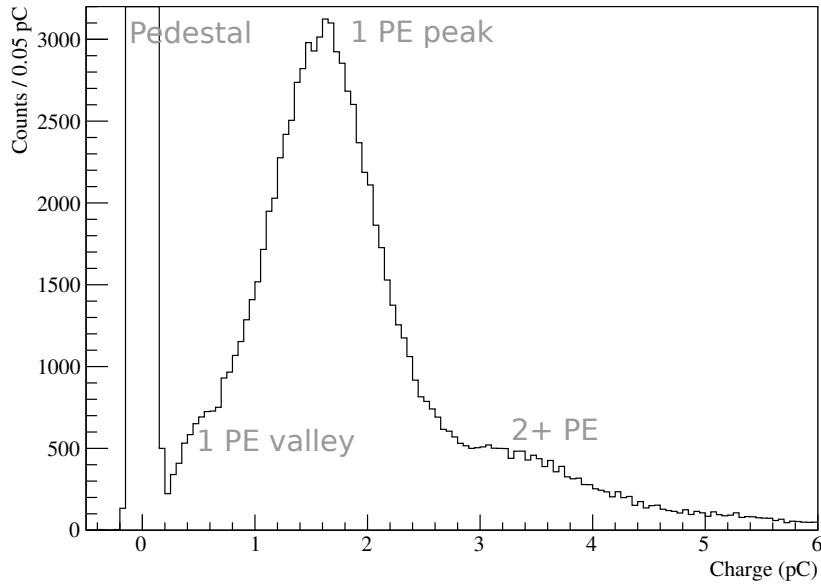


Figure 3. The charge distribution for PMT VA1206. The events around 0 pC correspond to baseline events with no photon detected. The SPE events peak around 1.6 pC and there is a small contribution for MPE events extending above 3 pC.

3.3.2 Timing

The Δt distribution for the PMT with serial number VA1206, running at a gain of 1×10^7 , is shown in Figure 4. The overall offset of Δt from zero is set by cable delays and is arbitrary. As discussed, because the trigger PMT has an extremely fast response, the Δt distribution is primarily showing the transit-time (TT) distribution for single photoelectrons detected by the measurement PMT. The width of the prompt light, peaking around 70 ns in the Δt distribution, can be fit with a Gaussian function to extract the transit-time spread (TTS).

Because the prompt TT distribution is not perfectly Gaussian (rather, it is slightly skewed right), the fit-range selected impacts the measured TTS distribution. After binning the Δt distribution in 0.2 ns bins, the peak is identified and a Gaussian is fit using a range that is ± 0.6 ns around the peak. The FWHM of the fitted Gaussian is taken to be the TTS of the PMT. By adjusting the fit range between 0.2 to 1.0 ns in steps of 0.2 ns, the fitted value of the TTS varies at most by 5%, which is the largest source of systematic uncertainty.

The values of the TTS are reported using the ± 0.6 ns range. The average TTS across the PMTs is 1.00 ns and the standard deviation is 0.08 ns. This indicates that these PMTs achieve a state-of-the-art timing resolution and that the behavior is very consistent from PMT to PMT.

In addition to the prompt light, there is a clear contribution of light that comes between 5 to 40 ns late, as identified in Fig. 4. This effect is due to elastic scatters of the PE off of the first dynode, before being accelerated back some time later. The fraction of detected photons that are late is quantified by identifying the prompt peak and integrating a window that is between 5 and 40 ns after the prompt peak and comparing that value to the integral of the full timing window.

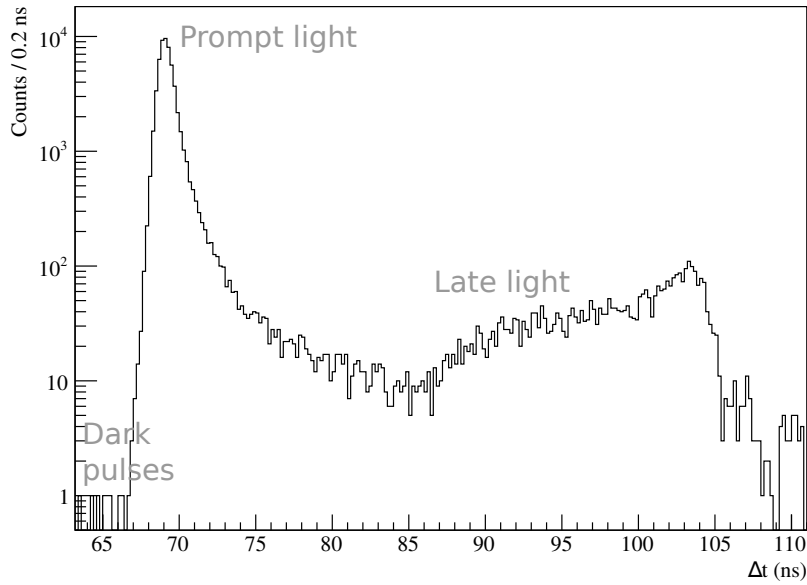


Figure 4. The Δt distribution for PMT VA1206. Note the offset in Δt from zero is set by cable delays and is arbitrary.

Averaging over all of the tested PMTs, the fraction of late-light is $9.39 \pm 0.58\%$.

3.3.3 High Voltage Scan

In order to determine the high voltage that yields a gain of 1×10^7 the high voltage is scanned across a range of values, and the gain is determined by measuring the mean of the charge distribution. For two PMTs, VA1293 and VA1300, we investigated the TTS and gain as a function of high voltage from 1650 V to 2500 V. The results are shown in Figure 5. Notably, at large gains of around 5×10^7 , reached with supply voltages around 2400 to 2500 V, the TTS is improved from around 1 ns to about 0.8 ns.

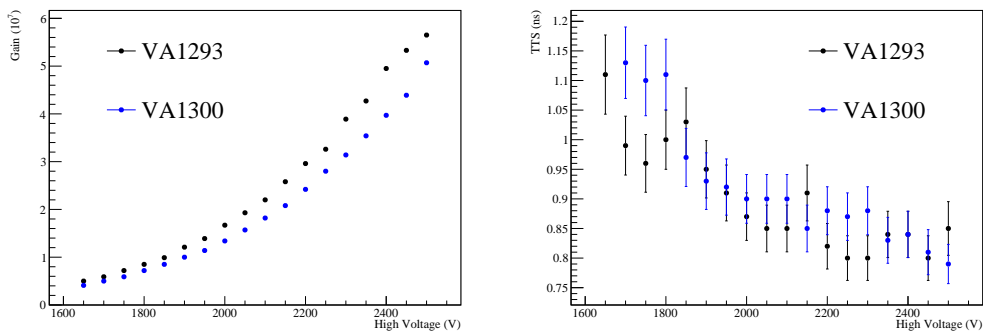


Figure 5. The gain (left) and TTS (right) as a function of the supply voltage for two PMTs. The uncertainties on the TTS include the statistical and systematic errors summed in quadrature.

3.3.4 Dark-Rate

The constrained timeline for the Eos construction and the installation of the PMTs restrained the total number of PMTs that could be dark-rate tested, but 14 PMTs were successfully tested. The dark-rate of the PMTs is measured at least twenty hours after the dark-box has been closed, allowing the PMT dark-rate to settle to baseline.

The rate is extracted by fitting a 50 ns pre-trigger window, prior to the Cherenkov light emission, with a flat polynomial. The total counts in that window is converted to a rate and is well-described by the uniform model. Over the 14 PMTs measured we find an average dark-rate of 2175 ± 1400 Hz, with a minimum rate of 590 Hz and a maximum rate of 5024 Hz. This level of variation is typical for large-area PMTs [14, 19].

The measurements are performed at room temperature around 22° C. The expected temperature of the water in Eos is 15° C, which would lead to an approximate decrease by a factor of 2-3 for the dark-rates [19, 20]. The measured dark-rates for these PMTs are similar to those reported for other large-area PMTs [12–16].

3.3.5 SPE summary

A summary of the SPE testing results is provided in Table 1. The SPE results for every PMT is provided in B.

Parameter	Mean	Maximum	Minimum
HV (V)	1989 ± 143	2500	1700
Charge P/V	5.69 ± 0.92	7.36	3.97
TTS (ns)	1.00 ± 0.08	1.23	0.83
Late-Fraction (%)	9.39 ± 0.58	11.2	7.46

Table 1. The mean, standard deviation, maximum, and minimum values of the measured SPE parameters for a gain of 1×10^7 .

4 Afterpulsing

Signal generated by residual ions inside of the PMT can cause delayed signals that occur hundreds of ns or several μ s after an initial PE. Specifically, a generated PE can ionize residual gases inside of the PMT, such as helium. The ions then slowly drift back to the photocathode, where they are absorbed, creating a single PE or multiple PEs that are delayed relative to the initial signal. The time-difference between the initial signal and the delayed signal is determined by the type of gas in the PMT, the electric field strength, and the size of the PMT. Notably, these afterpulses are produced via a different mechanism than what we call late-pulses in Section 3.3.2. For reference, the formation of afterpulses in large-area PMTs has been studied in Refs. [12, 21, 22].

4.1 Experimental Setup

A blue LED is directed at an R14688-100 PMT, operating at a gain of 10^7 , and pulsed at 100 Hz with a 30 ns pulse width. The amplitude of the pulse is adjusted to change the total amount of prompt

PE detected. Data is collected across a variety of different intensities to study the afterpulsing rate as a function of the number of PE in the prompt pulse.

The CAEN V1742 digitizer has a maximum window width of about $2 \mu\text{s}$, which was insufficient for measuring the afterpulses. Therefore, the afterpulsing setup digitized the PMT waveforms on a Lecroy Waverunner 9054 at 1 GS/s over a $50 \mu\text{s}$ window. The data is collected using custom software called `lecrunch` which outputs the waveforms to `hdf5` files.

4.2 Analysis

In order to identify the prompt pulse, generated by the LED light, and the subsequent afterpulses, the waveform is split into distinct windows. First, a $0.2 \mu\text{s}$ window at the beginning of the waveform is used to calculate the baseline. Then a $19.6 \mu\text{s}$ pre-trigger window is used to identify dark-pulses, in order to correct for their contribution in the afterpulsing window. A $0.4 \mu\text{s}$ window is used to identify the location of the prompt pulse and the following $29.8 \mu\text{s}$ is used to look for afterpulsing.

In the primary peak, where we expect the data to be MPE, the pulse is easily identified and integrated over a 60 ns window (centered around the peak). To roughly calculate the number of PE (NPE) detected in this window, the integrated charge is divided by the value of mean of the SPE charge distribution. The afterpulsing rate is then measured as a function of the NPE in the primary pulse.

The pulses in the dark-window and the afterpulsing window are identified by applying a 3 mV threshold and identifying threshold crossings. A threshold counting is only counted if the waveforms is below threshold on the previous sample. This threshold corresponds to roughly 0.2 PE .

4.3 Results

Five datasets are collected, varying the intensity of the LED. In the first dataset, the LED is dimly lit, with an average occupancy of around 2 PE . In the final dataset, the LED is pulsed such that the PMT has an average occupancy of almost 30 PE per pulse.

The time distribution of the afterpulses for one of the datasets, with an average occupancy of 5 PE , is shown in Figure 6. The afterpulsing distribution shows two clear peaks around 500 ns and $5.0 \mu\text{s}$ after the initial prompt light from the LED, which occurs at 0 ns in Figure 6. The locations and heights of each of these peaks reflects different gases at different amounts present in the PMT. By around $16.0 \mu\text{s}$ we no longer identify any afterpulsing above the dark noise background. The sharp cut-off at shorter times is due to the 400 ns window used to identify the hit-time of the prompt light, and it is possible some of the afterpulses with shorter times are not identified.

Most importantly, we study the afterpulsing rate as a function of the number of detected PE from the prompt LED light. These results are given in Figure 7. The figure shows the average number of afterpulses as a function of NPE, where a value of 0.5 indicates that in half of the events there was an afterpulse identified. A value larger than one would indicate more than one afterpulse per prompt LED pulse.

For the dimmest LED setting, with an integrated charge that indicates that we are primarily measuring one or two PE per LED pulse, the afterpulsing rate was about 2.5% . The linear fit indicates an average rate of 1.6% for an occupancy of 1 PE ; however, the fit clearly breaks down at very low occupancy, indicated by the negative value for the y-intercept. The linear fit is useful for interpolating and extrapolating to higher occupancy.

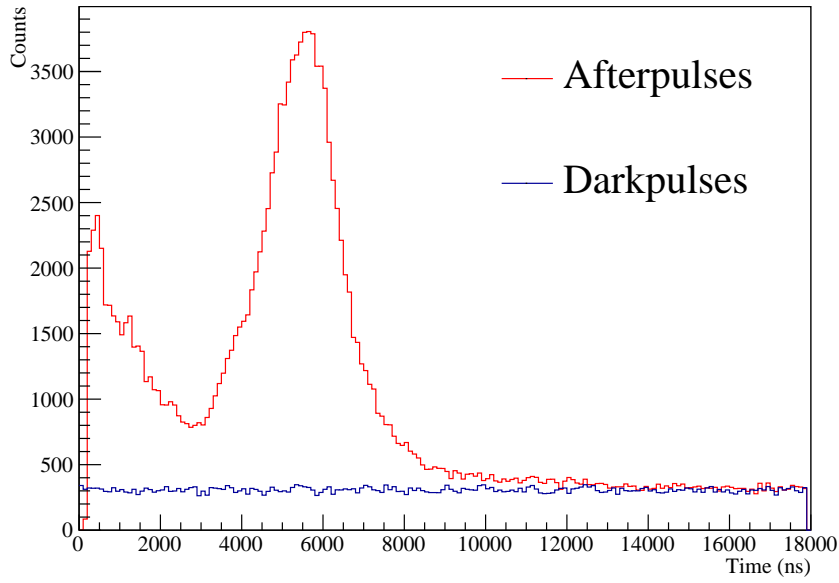


Figure 6. The timing distribution of the afterpulses for a dataset with an average occupancy of 5 PE. The events from the dark-rate, taken from a pre-trigger window, are shown as a direct comparison. The prompt light arrives at 0 ns for this figure.

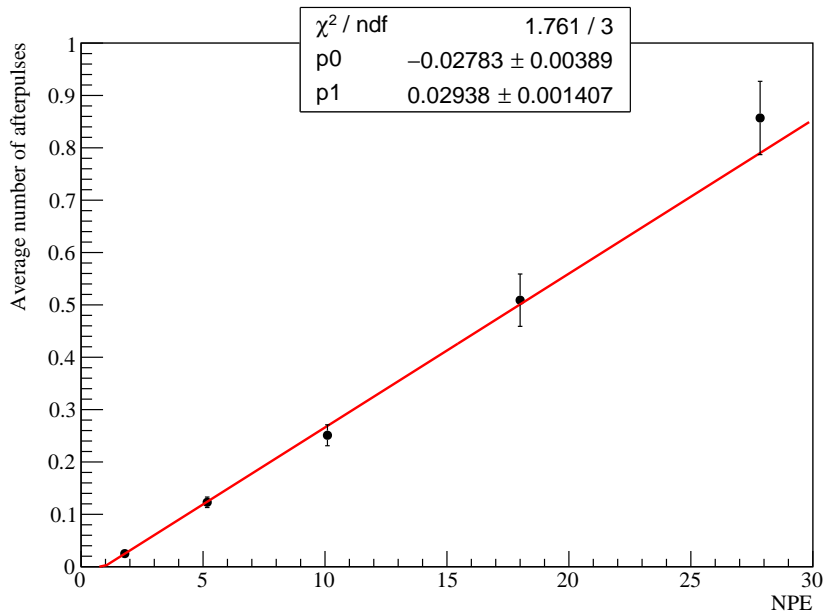


Figure 7. The average number of afterpulses detected for a given number of prompt NPE. A linear fit indicates that the average number of afterpulses produced for a 1 PE signal is 0.016.

It should be noted that the calculation of the average number of afterpulses does not include

several factors. First, no correction is made for an efficiency loss from the SPE selection, and a rough efficiency loss of 5% was estimated in Section 3.3.1. Second, any afterpulses with timing less than 400 ns are not included in this calculation, as discussed in relation to Figure 6. Again, we expect this to have a relatively small effect, as the 400 ns time-window is short relative to the 20 μ s window to identify afterpulses. Finally, we do not account for MPE afterpulses, and assume the pulses are SPE. To check this assumption, we look at the charge distribution of the afterpulses, and even at the highest LED intensity, we find only about 5% of the afterpulses are MPE.

5 Radiopurity Assay

PMTs are often a source of significant radioactive backgrounds in neutrino and dark-matter experiments [23]. This comes primarily from uranium and thorium intrinsic to the PMT glass and dynode that produces γ -rays that can travel through buffer material into the sensitive detector volume.

Samples taken from an intentionally broken R14688-100 PMT, provided by Hamamatsu, were sent to the low background counting facilities at the Black Hills Underground Campus. Measurements were performed on the 4850' level of the Sanford Underground Research Facility (SURF) [24–26] to measure the radioactivity of the PMT. The samples were broadly grouped in two categories: (1) the crushed glass from the PMT bulb and (2) the metallic and ceramic parts the make-up the dynode structure and the rest of the PMT. These two groups are measured separately in the SURF facilities using the Morgan detector station (see Ref. [24] for details). The results are provided in Table 2. The total weight of the glass and dynode parts is 0.51 kg and 0.39 kg respectively. Notably, Hamamatsu communicated that the glass for these PMTs is possible to construct with lower radioactivity [27].

Sample	U (mBq/kg)	Th (mBq/kg)	K (mBq/kg)
PMT glass	3144 ± 158	4486 ± 257	7874 ± 398
PMT dynode	421.2 ± 28.2	55.8 ± 5.0	219 ± 24

Table 2. The results of the radiological assay of the PMT parts, performed at SURF.

6 Discussion

Based on the results shown in this manuscript, the R14688-100 is a promising candidate for future large-scale neutrino experiments, such as Theia, that hope to utilize fast timing to improve background rejection [6]. Additionally, existing detectors with planned upgrades that already utilize 8-inch PMTs, such as SNO+ [28], could directly replaced old PMTs with these modern PMTs. This improvement would more than double the detection efficiency and improve the TTS by more than a factor of three [29].

Additionally, the ability to identify the number of photons detected by a PMT will be important for future scintillation based neutrino detectors [30]. This would help improve energy resolution by providing a more precise measure of the total light detected. Thus, the ability to distinguish one PE from zero, two PE from one PE, etc. will be an important aspect of future photosensors.

Given the large P/V ratio measured in this manuscript, the R14688-100 PMT provides excellent discrimination capability for PE counting.

The timing of the R14688-100 PMT, measured to be on average around 1 ns (FWHM) across 206 PMTs, is the primary motivation for using this large-area PMT. This state-of-the-art timing is at least twice as good as other large-area PMTs, and could significantly improve reconstruction performance and background rejection in future scintillation-based neutrino experiments [31]. About 10% of the light is detected late relative to the prompt peak, which is typical for large-area PMTs. The dark-rate of the PMTs has not been robustly characterized at the temperatures standard for large detectors; however, initial measurements of several PMTs at room temperature indicate dark-rates consistent with other PMTs of similar sizes. Lastly, we performed an afterpulsing measurement of a single PMT, which indicated afterpulsing rates around 2% per PE, with peaks in the timing distribution around 500 ns and 5 μ s.

7 Conclusion

In this manuscript the SPE detection performance is characterized for 206 large-area Hamamatsu R14688-100 PMTs. The fast timing and excellent P/V makes it an ideal PMT for use in Eos, where these features will be used to perform Cherenkov and scintillation separation and precision photon counting. Ultimately, this will help improve reconstruction and reduce backgrounds. These measurements can also be directly input into simulation software in order to better simulate the detector response. Finally, measurements made of afterpulsing rate, dark-rate, and radioactivity of the PMT provide important details for Eos and for future experiments deciding on the type of PMT to use.

Data Availability Statement

The data used in this manuscript is available in an accessible `postgres` database hosted at Lawrence Berkeley National Lab. If interested, please contact the author for database connection information. The results for the full list of all tests performed on the Eos PMT is available at <https://nino.lbl.gov/pmts/>.

8 Acknowledgements

Thank you kindly to Brianna Mount and Douglas Tiedt for performing the background counting measurements and analysis at the Black Hills State University Underground Campus and the Berkeley Low Background Facility. The work conducted at Lawrence Berkeley National Laboratory was performed under the auspices of the U.S. Department of Energy under Contract DE-AC02-05CH11231. This project was funded by the U.S. Department of Energy, National Nuclear Security Administration, Office of Defense Nuclear Nonproliferation Research and Development (DNN R&D). Author M. Duce was supported by the Department of Energy and National Nuclear Security Administration, United States through the Enabling Technology and Innovation Consortium under Award Number DE-NA0003921.

A Magnetic Shielding Tests

The performance of PMTs is known to be affected by even weak ambient magnetic fields, such as that of the Earth's. These magnetic fields deflect the electron trajectories via the Lorentz force, and tend to decrease the overall PE collection efficiency of the PMT. Thus, flexible magnetic shielding, such as FINEMET[®], that extends around the PMT can be used to improve the overall detection efficiency [32].

In this section, we investigate two different designs for a flexible magnetic shielding and test the impact on the PMT collection efficiency. Figure 8 shows one of the magnetic shielding designs, and the second design is very similar with the slant height reduced to 14 cm. These designs are based on the those presented in Ref. [32], which studied the impact of FINEMET magnetic shielding on the 8-inch PMTs used in the Daya Bay experiment.

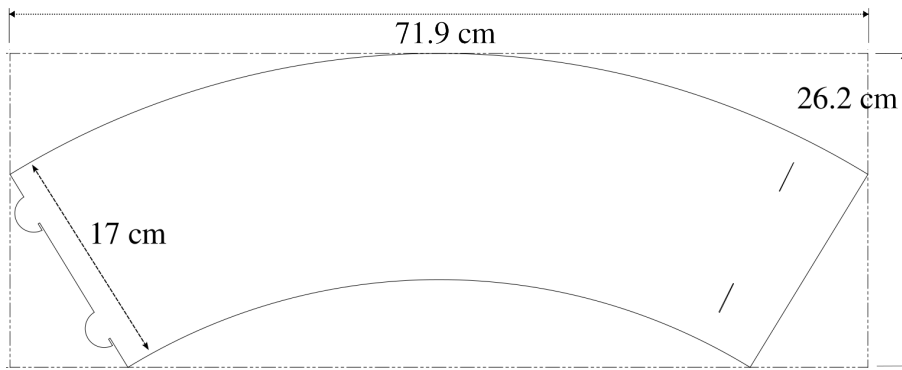


Figure 8. Two dimensional pattern of one of the conical magnetic shielding designs that was tested, based on the designs used for the Daya Bay experiment [32].

The focus of the magnetic shielding testing is for applications in Eos and therefore only a handful of configurations are run. More complete magnetic shielding tests on similar PMTs, such as those conducted in Refs. [32], [16], and [14], use externally applied magnetic fields to look at the changing efficiency as a function of magnetic field strength. Here we primarily focus on the impact of the magnetic shielding when shielding only against the Earth's magnetic field. Therefore, these tests are not general performance characterization as a function of magnetic field strength, but rather a handful of configurations relevant for Eos, that provide some useful context for future detectors as well.

In the SPE experimental setup (shown in Figure 2) the photomultiplier tubes are wrapped in the FINEMET magnetic shielding. However, the gain and TTS of the PMT are measured both with and without magnetic shielding and no significant change is identified in our setup. Tests performed to understand changes to the PMT detection efficiency are described in the following sections.

A.1 Experimental Setup

The setup designed to test changes in the PMT efficiency consists of a blue LED pointed at a dichroic filter, which splits the light towards two different PMTs. Directly behind the dichroic filter is an R14688-100 'measurement' PMT. At 90 degrees from the filter is a H11934-200 1-inch

‘monitoring’ PMT (the same PMT used as the trigger PMT in the SPE setup). The monitoring PMT is used to measure the relative intensity of the light to normalize across different trials. This is necessary as the intensity of the LED drifts slightly, as its temperature changes.

The LED is pulsed with 25 ns pulse width at 100 Hz, using a function generator with an intensity such that the measurement PMT detects around 50 PEs per pulse. The high intensity is useful to measure small relative changes in efficiency, which would effectively shift the total number of PEs detected in each pulse from the LED. A total of 100,000 events are collected in each trial. The pulse from the function generator is split and also used to trigger the DAQ. The DAQ system is identical to that described in Section 3.1.

Measurements are performed with the two different magnetic shielding designs and with no magnetic shielding around the measurement PMT. Due to the orientation of the darkbox, the PMTs are placed pointing 10 degrees off of north-south. With respect to this positioning, the magnetic field is measured at the front-face of the PMT (no magnetic shielding) to be 32 μT up-down, 34 μT left-right, and 12 μT in-out. With the magnetic shielding, each component is reduced by more than a factor of five.

A.2 Analysis

The PMT pulses from both the measurement and monitoring PMT are integrated using 60 ns windows, with baselines estimated in a 40 ns pre-trigger window. The width of the integration window is set to capture the full width of the PMT pulse for both PMTs. The metric used to measure the efficiency change across configurations is the total integrated charge at the measurement PMT, Q , normalized by the integrated charge at the monitoring PMT, Q_m , $\epsilon = Q/Q_m$.

A.3 Results

Measurements of ϵ are collected across several trials for each of the three configurations, as detailed in Table 3. The different trials are run under identical conditions, but after removing and replacing the magnetic shielding (if applicable) and ramping the high voltage down and then back up, in order to understand the measurement systematics. Six of the trials are performed with one of the 14 cm slant height magnetic shielding design, where the systematics are most robustly tested. Across the runs in the same configuration, there is at most a 3% variation in the value of ϵ , as identified in Table 3 in the trials with the 14 cm slant height design.

Notably, the value of ϵ does not change between the different configurations, indicating no increase or decrease in the overall collection efficiency from using the magnetic shielding. This indicates shielding of the ambient magnetic fields generated by the Earth is not effective for increasing the collection efficiency of this particular PMT. However, these results are specific to the magnetic field strength at the particular location the tests were run. Because the primary goal was to determine if individual PMT magnetic shielding was necessary for Eos, the lack of any clear significant impact in these tests led to the decision to remove individual shielding components around each PMT.

Q (pC)	Q_m (pC)	ϵ	Slant Height (cm)	Trial
75.91	12.26	6.19	0	1
76.74	12.36	6.20	0	2
76.80	12.45	6.17	0	3
76.48	12.39	6.17	14	1
76.89	12.60	6.10	14	2
78.24	12.69	6.17	14	3
78.88	12.64	6.24	14	4
79.68	12.86	6.20	14	5
79.98	12.75	6.27	14	6
81.80	13.19	6.20	17	1
82.88	13.32	6.22	17	2

Table 3. The results of the magnetic shielding tests with varying magnetic shield designs, using PMT VA1166. ϵ is constant within the expected 3% systematic uncertainty.

B List of Results for All PMTs

Table 4 provides a list of the high voltage, charge peak, charge peak-to-valley, TTS, and late-pulsing percentage for all PMTs tested in the SPE setup.

PMT ID	High Voltage	Q Peak [pC]	Q P/V	TTS [ns]	Late-light Pct. (%)
VA1059	1960	1.54	5.62	1.035	8.81
VA1060	2395	1.62	5.29	0.835	8.83
VA1062	1980	1.54	5.53	0.915	8.98
VA1064	1865	1.58	5.75	0.985	8.96
VA1065	1950	1.62	4.87	1.008	9.27
VA1066	1875	1.57	5.36	1.053	9.82
VA1067	1935	1.57	4.76	1.038	9.64
VA1068	1720	1.58	4.32	1.115	9.18
VA1070	1900	1.52	4.59	1.226	8.18
VA1071	1900	1.59	3.97	1.113	9.03
VA1072	1830	1.61	5.24	0.975	9.17
VA1073	1950	1.59	4.68	1.014	9.18
VA1074	1900	1.56	5.85	1.056	9.79
VA1075	1920	1.49	6.84	1.020	8.89
VA1076	1900	1.62	5.89	1.091	9.45
VA1077	1850	1.54	4.73	1.137	8.51
VA1078	1800	1.57	5.71	1.137	8.76
VA1080	1845	1.56	5.11	1.044	8.58
VA1081	1700	1.58	5.80	1.108	8.12
VA1082	1705	1.58	5.24	1.107	8.43
VA1084	1940	1.56	6.73	1.041	8.93
VA1086	1955	1.56	6.08	1.017	8.84
VA1088	2040	1.63	6.48	0.932	9.88
VA1089	1790	1.58	5.64	1.101	9.51
VA1090	1840	1.56	6.05	1.165	8.73
VA1091	1820	1.57	7.15	1.113	8.73
VA1092	1810	1.59	6.33	1.045	8.16
VA1093	1745	1.57	6.09	1.188	9.20
VA1094	1725	1.62	6.09	1.149	9.44
VA1095	1720	1.61	4.96	1.011	8.86
VA1097	2020	1.68	6.98	0.976	9.17
VA1098	2105	1.57	5.68	0.987	9.10
VA1099	1980	1.58	6.58	0.928	9.82
VA1100	2100	1.55	4.94	0.958	9.19
VA1101	1860	1.62	5.42	1.134	9.42
VA1102	1925	1.60	6.07	1.087	10.14
VA1103	1950	1.58	6.39	1.030	9.35

VA1104	2080	1.61	5.56	0.946	9.94
VA1105	2050	1.56	5.77	0.942	9.62
VA1106	1955	1.59	5.70	0.975	10.05
VA1107	1895	1.52	5.98	1.011	9.86
VA1108	2020	1.59	5.64	1.004	9.97
VA1110	1980	1.55	6.26	0.988	10.38
VA1111	2150	1.56	6.95	1.019	9.55
VA1113	1840	1.60	6.82	1.043	9.98
VA1114	1880	1.58	6.36	1.041	9.86
VA1115	1870	1.58	6.47	1.030	9.91
VA1116	2070	1.59	5.62	0.970	10.01
VA1117	2085	1.63	5.76	0.992	9.87
VA1119	1825	1.63	5.48	1.114	9.60
VA1120	2110	1.55	5.71	0.885	9.65
VA1121	1915	1.61	5.81	1.057	9.67
VA1123	1845	1.62	7.16	1.020	9.86
VA1124	1790	1.61	6.90	1.106	9.64
VA1125	1900	1.66	6.09	0.974	10.34
VA1126	1935	1.56	5.80	1.109	9.53
VA1127	1870	1.56	6.62	1.039	9.64
VA1128	1955	1.62	5.53	1.001	9.65
VA1129	1915	1.55	6.76	1.118	9.94
VA1130	1865	1.56	7.14	1.060	9.82
VA1131	1945	1.60	6.31	0.975	10.10
VA1132	1825	1.56	6.13	1.087	9.16
VA1134	2030	1.56	5.74	0.970	10.38
VA1135	1860	1.63	6.95	1.008	9.77
VA1136	2010	1.62	5.79	1.095	10.93
VA1137	2025	1.73	6.59	1.072	11.17
VA1138	2100	1.69	6.18	1.005	10.15
VA1139	1955	1.69	6.18	1.005	10.15
VA1140	2100	1.60	5.76	0.977	9.83
VA1141	1945	1.63	6.48	1.002	9.99
VA1142	2160	1.54	5.78	0.864	9.46
VA1143	2220	1.80	5.40	1.011	10.29
VA1144	1930	1.55	5.09	1.105	9.40
VA1145	2065	1.62	5.74	1.000	10.66
VA1146	1995	1.55	5.80	1.018	9.79
VA1148	1980	1.56	5.53	0.997	10.08
VA1149	2045	1.52	6.03	1.010	10.24
VA1150	1870	1.60	5.91	1.033	9.64
VA1151	1930	1.51	5.67	1.164	9.61
VA1252	2095	1.53	6.12	0.908	9.77

VA1154	1990	1.59	6.31	0.983	9.37
VA1155	2050	1.53	6.14	1.101	9.40
VA1156	2015	1.59	6.23	0.947	9.95
VA1157	2170	1.55	5.03	0.897	9.43
VA1158	2150	1.55	5.96	0.946	9.71
VA1159	1920	1.58	6.29	1.072	9.06
VA1160	1900	1.56	5.73	1.059	9.26
VA1161	1905	1.54	5.37	0.961	9.42
VA1162	2150	1.66	5.26	0.834	10.27
VA1164	2130	1.64	5.70	0.938	9.54
VA1165	2035	1.61	6.22	0.978	8.60
VA1166	2190	1.54	6.02	0.841	9.65
VA1168	1900	1.59	7.26	1.035	9.18
VA1170	2265	1.65	6.57	0.921	9.74
VA1172	2280	1.52	4.24	0.911	8.56
VA1173	2200	1.52	5.51	0.953	9.29
VA1174	2060	1.60	6.52	0.921	8.91
VA1175	2060	1.63	4.43	1.026	7.46
VA1176	2150	1.63	6.20	0.853	9.77
VA1177	2040	1.61	7.27	0.919	9.61
VA1178	2040	1.48	5.37	0.922	9.40
VA1179	2040	1.68	5.42	0.987	9.72
VA1180	2255	1.62	5.30	0.939	9.60
VA1181	2180	1.60	6.01	0.878	9.35
VA1182	2350	1.31	4.60	0.924	8.78
VA1183	2010	1.45	6.42	0.912	9.24
VA1184	1980	1.52	5.83	0.980	9.02
VA1185	1955	1.64	6.25	0.959	9.75
VA1186	1995	1.59	5.88	0.974	9.27
VA1187	1925	1.55	5.37	0.918	9.60
VA1188	2165	1.50	5.40	0.929	9.37
VA1189	2100	1.57	4.99	0.933	9.85
VA1190	2050	1.60	5.75	1.016	9.40
VA1191	2180	1.56	5.43	0.969	9.22
VA1192	1955	1.53	6.47	0.927	9.00
VA1193	2080	1.56	5.76	1.075	9.44
VA1195	1720	1.60	6.46	1.123	9.14
VA1196	2500	1.50	4.75	0.920	9.57
VA1197	2220	1.52	5.17	0.968	8.59
VA1202	2310	1.46	4.43	0.846	8.99
VA1205	2260	1.59	4.44	0.939	9.11
VA1206	2110	1.60	4.58	0.914	9.25
VA1207	2110	1.78	5.20	0.895	9.82

VA1208	2290	1.62	5.18	0.874	10.02
VA1213	2205	1.54	4.54	0.880	9.41
VA1215	1935	1.54	4.05	0.934	9.17
VA1216	2020	1.67	4.94	0.945	9.17
VA1217	2125	1.53	5.10	0.989	8.60
VA1218	2015	1.51	5.16	1.025	9.60
VA1220	2040	1.51	5.15	1.062	9.32
VA1223	2025	1.65	4.51	1.023	9.66
VA1224	1950	1.55	5.69	0.974	9.30
VA1225	1800	1.62	5.50	1.093	9.55
VA1226	2015	1.54	6.02	1.017	9.11
VA1227	1860	1.51	6.85	1.028	9.36
VA1228	1850	1.56	5.46	1.120	8.85
VA1229	1865	1.50	5.01	1.101	8.97
VA1230	2050	1.73	7.36	0.911	9.17
VA1231	1980	1.66	5.11	0.917	9.30
VA1232	2425	1.70	4.76	0.845	9.05
VA1233	2170	1.51	6.61	0.935	9.67
VA1235	2105	1.48	4.67	0.892	7.27
VA1237	1910	1.61	5.53	1.037	9.47
VA1238	1790	1.52	4.52	0.979	8.75
VA1239	2050	1.57	4.72	1.022	9.38
VA1240	1810	1.54	5.45	1.063	8.86
VA1241	1980	1.67	5.26	0.926	9.19
VA1242	2045	1.60	5.86	0.946	9.94
VA1243	2045	1.61	6.30	1.012	9.35
VA1244	2100	1.49	4.81	0.866	8.91
VA1245	1945	1.64	5.23	1.063	8.80
VA1246	1900	1.52	5.03	0.978	8.43
VA1247	2075	1.52	4.85	0.934	8.05
VA1248	1920	1.57	5.52	1.049	10.04
VA1249	1860	1.49	5.58	0.951	8.68
VA1251	2095	1.49	4.85	0.988	9.11
VA1252	2095	1.53	6.12	0.908	9.77
VA1253	1930	1.50	5.40	1.024	9.08
VA1254	2005	2.00	6.65	0.986	10.06
VA1255	2020	1.58	5.92	0.969	10.21
VA1256	2075	1.59	5.65	0.852	9.05
VA1257	2170	1.49	6.09	1.012	10.36
VA1258	1910	1.55	5.04	0.968	10.02
VA1259	1810	1.66	6.17	1.064	10.28
VA1260	2230	1.61	6.17	0.953	10.51
VA1263	1925	1.59	5.17	0.976	8.66

VA1264	1880	1.54	6.33	1.010	10.21
VA1265	2350	1.66	7.38	0.791	7.53
VA1266	1980	1.58	5.46	1.050	9.60
VA1267	1990	1.58	5.27	0.882	9.24
VA1268	1850	1.49	5.08	0.972	8.55
VA1269	2180	1.59	6.19	0.949	10.29
VA1270	1970	1.54	4.76	0.895	9.30
VA1271	1820	1.51	4.96	1.006	8.79
VA1272	2000	1.59	5.95	0.962	10.61
VA1273	2110	1.61	6.32	0.902	11.64
VA1274	1955	1.59	4.99	0.946	9.33
VA1276	2230	1.56	4.62	0.873	8.96
VA1277	2095	1.53	5.15	0.867	9.36
VA1278	2155	1.59	5.46	0.890	9.40
VA1279	2085	1.65	5.83	0.934	9.01
VA1280	1810	1.62	6.05	1.192	8.66
VA1281	1905	1.58	5.54	1.082	8.72
VA1283	2040	1.52	4.74	0.919	9.54
VA1284	1880	1.59	5.72	0.970	8.56
VA1285	2190	1.55	5.38	0.936	9.62
VA1286	1890	1.61	4.77	0.991	9.30
VA1287	1975	1.56	4.36	0.928	9.17
VA1288	2065	1.58	5.65	0.878	9.23
VA1289	2030	1.49	4.88	0.911	9.55
VA1290	2070	1.53	5.62	0.950	8.94
VA1291	1865	1.57	5.67	1.030	8.80
VA1293	1845	1.58	5.37	0.952	8.22
VA1295	1880	1.60	5.59	0.999	9.26
VA1298	1855	1.64	5.64	1.000	9.90
VA1299	2035	1.60	5.30	0.939	9.96
VA1300	1900	1.57	5.00	1.026	8.92
VA1301	1790	1.62	5.68	1.126	8.63
VA1302	1975	1.58	5.67	1.008	8.72
VA1303	1805	1.57	5.92	1.074	8.37
VA1305	1855	1.64	4.83	1.118	8.48
VA1307	1745	1.54	5.33	1.171	8.64
VA1309	1840	1.65	5.28	1.083	9.52
VA1312	1905	1.60	5.30	1.117	8.23
VA1313	1805	1.58	5.16	1.134	8.25
VA1314	1770	1.56	5.23	1.145	8.07

Table 4: All of the SPE characterization results at a gain of 1×10^7 .
The TTS is the FWHM.

References

1. Ahmad, Q. R. *et al.* Direct evidence for neutrino flavor transformation from neutral current interactions in the Sudbury Neutrino Observatory. *Phys. Rev. Lett.* **89**, 011301. arXiv: [nucl-ex/0204008](#) (2002).
2. Fukuda, Y. *et al.* Evidence for oscillation of atmospheric neutrinos. *Phys. Rev. Lett.* **81**, 1562–1567. arXiv: [hep-ex/9807003](#) (1998).
3. Arpesella, C. *et al.* Direct Measurement of the Be-7 Solar Neutrino Flux with 192 Days of Borexino Data. *Phys. Rev. Lett.* **101**, 091302. arXiv: [0805.3843 \[astro-ph\]](#) (2008).
4. Ajaj, R. *et al.* Search for dark matter with a 231-day exposure of liquid argon using DEAP-3600 at SNOLAB. *Phys. Rev. D* **100**, 022004. arXiv: [1902.04048 \[astro-ph.CO\]](#) (2019).
5. An, F. P. *et al.* Observation of electron-antineutrino disappearance at Daya Bay. *Phys. Rev. Lett.* **108**, 171803. arXiv: [1203.1669 \[hep-ex\]](#) (2012).
6. Askins, M. *et al.* THEIA: an advanced optical neutrino detector. *Eur. Phys. J. C* **80**, 416. arXiv: [1911.03501 \[physics.ins-det\]](#) (2020).
7. Wen, L.-J. *et al.* A quantitative approach to select PMTs for large detectors. *Nucl. Instrum. Meth. A* **947**, 162766. arXiv: [1903.12595 \[physics.ins-det\]](#) (2019).
8. Anderson, T. *et al.* Eos: conceptual design for a demonstrator of hybrid optical detector technology. *JINST* **18**, P02009. arXiv: [2211.11969 \[physics.ins-det\]](#) (2023).
9. Kaptanoglu, T., Luo, M., Land, B., Bacon, A. & Klein, J. Spectral Photon Sorting For Large-Scale Cherenkov and Scintillation Detectors. *Phys. Rev. D* **101**, 072002. arXiv: [1912.10333 \[physics.ins-det\]](#) (2020).
10. Yeh, M. *et al.* A new water-based liquid scintillator and potential applications. *Nucl. Instrum. Meth. A* **660**, 51–56 (2011).
11. Biller, S. D., Leming, E. J. & Paton, J. L. Slow fluors for effective separation of Cherenkov light in liquid scintillators. *Nucl. Instrum. Meth. A* **972**, 164106. arXiv: [2001.10825 \[physics.ins-det\]](#) (2020).
12. Kaptanoglu, T. Characterization of the Hamamatsu 8” R5912-MOD Photomultiplier Tube. *Nucl. Instrum. Meth. A* **889**, 69–77. arXiv: [1710.03334 \[physics.ins-det\]](#) (2018).
13. Hamamatsu. *Photomultiplier tube R14688-100: Hamamatsu Photonics* https://www.hamamatsu.com/us/en/product/optical-sensors/pmt/pmt_tube-alone/head-on-type/R14688-100.html. [Accessed June 15, 2023]. 2023.
14. Brack, J. *et al.* Characterization of the Hamamatsu R11780 12 inch Photomultiplier Tube. *Nucl. Instrum. Meth. A* **712**, 162–173. arXiv: [1210.2765 \[physics.ins-det\]](#) (2013).
15. Lei, X.-C. *et al.* Evaluation of new large area PMT with high quantum efficiency. *Chin. Phys. C* **40**, 026002. arXiv: [1504.03174 \[physics.ins-det\]](#) (2016).
16. Barros, N. *et al.* Characterization of the ETEL D784UKFLB 11 in. photomultiplier tube. *Nucl. Instrum. Meth. A* **852**, 15–19. arXiv: [1512.06916 \[physics.ins-det\]](#) (2017).

17. Askins, M. *et al.* *ratpac-two* <https://github.com/rat-pac/ratpac-two>. 2023.
18. Hamamatsu. *Datasheet for R11265U SERIES / H11934 SERIES* [Accessed June 16, 2022]. 2019.
19. Akindele, O. A. *et al.* Acceptance tests of Hamamatsu R7081 photomultiplier tubes. arXiv: [2306.09926 \[physics.ins-det\]](https://arxiv.org/abs/2306.09926) (2023).
20. Hamamatsu. *Photomultiplier Tubes, Basics and Application, Fourth Addition* https://www.hamamatsu.com/content/dam/hamamatsu-photonics/sites/documents/99_SALES_LIBRARY/etd/PMT_handbook_v4E.pdf. [Accessed Aug. 10, 2023]. 2023.
21. Akchurin, N. & Kim, H. A study on ion initiated photomultiplier afterpulses. *Nucl. Instrum. Meth. A* **574**, 121–126. ISSN: 0168-9002. <https://www.sciencedirect.com/science/article/pii/S0168900207001532> (2007).
22. Ma, K. *et al.* Time and amplitude of afterpulse measured with a large size photomultiplier tube. *Nucl. Instrum. Meth. A* **629**, 93–100. <https://doi.org/10.1016%2Fj.nima.2010.11.095> (2011).
23. Akerib, D. S. *et al.* An Ultra-Low Background PMT for Liquid Xenon Detectors. *Nucl. Instrum. Meth. A* **703**, 1–6. arXiv: [1205.2272 \[physics.ins-det\]](https://arxiv.org/abs/1205.2272) (2013).
24. Tiedt, D., Mount, B. & Rodriguez, A. Counting facilities at the Black Hills Underground Campus. *AIP Conference Proceedings* **2908**, 020003. ISSN: 0094-243X. eprint: https://pubs.aip.org/aip/acp/article-pdf/doi/10.1063/5.0161194/18110386/020003_1_5.0161194.pdf. <https://doi.org/10.1063/5.0161194> (Sept. 2023).
25. Akerib, D. S. *et al.* The LUX-ZEPLIN (LZ) radioactivity and cleanliness control programs. *Eur. Phys. J. C* **80**. [Erratum: *Eur.Phys.J.C* 82, 221 (2022)], 1044. arXiv: [2006.02506 \[physics.ins-det\]](https://arxiv.org/abs/2006.02506) (2020).
26. Aalbers, J. *et al.* Background determination for the LUX-ZEPLIN dark matter experiment. *Phys. Rev. D* **108**, 012010. arXiv: [2211.17120 \[hep-ex\]](https://arxiv.org/abs/2211.17120) (2023).
27. Hamamatsu. private communication.
28. Albanese, V. *et al.* The SNO+ experiment. *JINST* **16**, P08059. arXiv: [2104.11687 \[physics.ins-det\]](https://arxiv.org/abs/2104.11687) (2021).
29. Biller, S., Jelley, N., Thorman, M., Fox, N. & Ward, T. Measurements of photomultiplier single photon counting efficiency for the Sudbury Neutrino Observatory. *Nucl. Instrum. Meth. A* **432**, 364–373. ISSN: 0168-9002. <https://www.sciencedirect.com/science/article/pii/S0168900299005008> (1999).
30. Akashi-Ronquest, M. *et al.* Improving Photoelectron Counting and Particle Identification in Scintillation Detectors with Bayesian Techniques. *Astropart. Phys.* **65**, 40–54. arXiv: [1408.1914 \[physics.ins-det\]](https://arxiv.org/abs/1408.1914) (2015).
31. Land, B. J. *et al.* MeV-scale performance of water-based and pure liquid scintillator detectors. *Phys. Rev. D* **103**, 052004. arXiv: [2007.14999 \[physics.ins-det\]](https://arxiv.org/abs/2007.14999) (2021).
32. Chen, M. *et al.* Development of a magnetic shield for 20-inch microchannel plate photomultiplier tubes. *Nucl. Instrum. Meth. A* **1039**, 167128 (2022).